Journal of Alloys and Compounds, 191 (1993) 53–62
JALCOM 450

Electronic structure of $ZrNi_4P_2$ and related compounds with $ZrFe_4Si_2$-type structure

A. Le Beuze, M. C. Zerrouki and R. Lissillour
Laboratoire de Chimie Théorique, UA CNRS 1495, Université de Rennes I, Avenue du Général Leclerc, F-35042 Rennes Cédex (France)

R. Guérin
Laboratoire de Chimie Minérale B, UA CNRS 1495, Université de Rennes I, Avenue du Général Leclerc, F-35042 Rennes Cédex (France)

W. Jeitschko
Anorganisch-Chemisches Institut der Universität, Wilhelm-Klemm-Strasse 8, W-4400 Münster (Germany)

(Received 27 July, 1992)

Abstract

Extended Hückel molecular orbital and tight-binding band structure calculations have been performed on $ZrNi_4P_2$ and then applied through a rigid band model to related compounds with the same $ZrFe_4Si_2$-type structure. The electronic structure has been built up step by step, from fragments, in order to obtain a better understanding of the main interactions which govern the evolution of the lengths of the metal-metal bonds and the lattice cohesion. The role of the 3d metal electron count and that of the ligand matrix are displayed and discussed. The bonding character between the zirconium cation and the covalent system $|Ni_4P_2|$ is also studied in some detail.

1. Introduction

The ternary compound $ZrNi_4P_2$ was the first phosphide reported to crystallize with the $ZrFe_4Si_2$-type structure [1]. The crystal structure of $ZrNi_4P_2$ was refined previously from powder and more recently from single-crystal data [2, 3]. As frequently observed for numerous structure types such as $Zr_2Fe_{12}P_7$, $Zr_6Ni_{20}P_{13}$ and Zr_2NiP_2 [4–6], the substitution of zirconium by a rare earth in $ZrNi_4P_2$ led to a new series of ternary phosphides $LnNi_4P_2$ (Ln ≡ Y, Gd–Lu) [7]. Subsequently the corresponding arsenides $LnNi_4As_2$ [3, 8] as well as iron- or manganese-containing phosphides $ZrFe_4P_2$, $ScFe_4P_2$ and UMn_4P_2 were synthesized [8]. Structure refinements of $TbNi_4P_2$, $DyNi_4As_2$ and $ScFe_4P_2$ have been reported [7, 8]. As seen in Fig. 1, where the crystal structure of $ZrNi_4P_2$ is drawn in a projection onto the |001| plane, the main feature of the compounds with the $ZrFe_4Si_2$-type structure is the tetrahedral M_4 clusters (M is a 3d transition element) which are fused to form linear chains by sharing common edges along the |001| direction. However, important variations occur from one compound to the other in the lengths of intracluster (d_1, d_2) and intercluster (d_3) metal–metal bonds and metal–ligand (d_4, d_5) bonds. The unit cell parameters and the main interatomic distances are given in Table 1. As an example, the metal–metal distances increase as $d_3 < d_1 < d_2$ for ternary phosphides $M'Ni_4P_2$ (M′ ≡ Zr, Tb) contrary to what is observed for $DyNi_4As_2$ ($d_2 < d_1 < d_3$). In the case of the iron-containing compounds $ScFe_4P_2$ and $ZrFe_4Si_2$, this order is again different.

Magnetic measurements performed between 4 and 300 K on $ZrNi_4P_2$ revealed quite a temperature-independent susceptibility ($\chi_m = 0.000\,45$ emu mol^{-1} at 300 K) which indicates Pauli paramagnetism of the conduction electrons. The metallic behaviour of $ZrNi_4P_2$ has been confirmed by electrical measurements on sintered powders [9]. Thereby the ternary $ZrNi_4P_2$ can be written as $Zr^{4+}|Ni_4P_2|^{4-}$. In the same manner, magnetic measurements on $LnNi_4As_2$ compounds above 50 K indicate a Curie–Weiss paramagnetic behaviour with effective moments in good agreement with those expected for the free Ln^{3+} ions, except for ytterbium for which a divalent character is observed [9]. Thus the $LnNi_4As_2$ compounds can be expressed as $Ln^{3+}|Ni_4As_2|^{3-}$, especially $Dy^{3+}|Ni_4As_2|^{3-}$, and by extension the electronic configurations can be deduced

0925-8388/93/$6.00

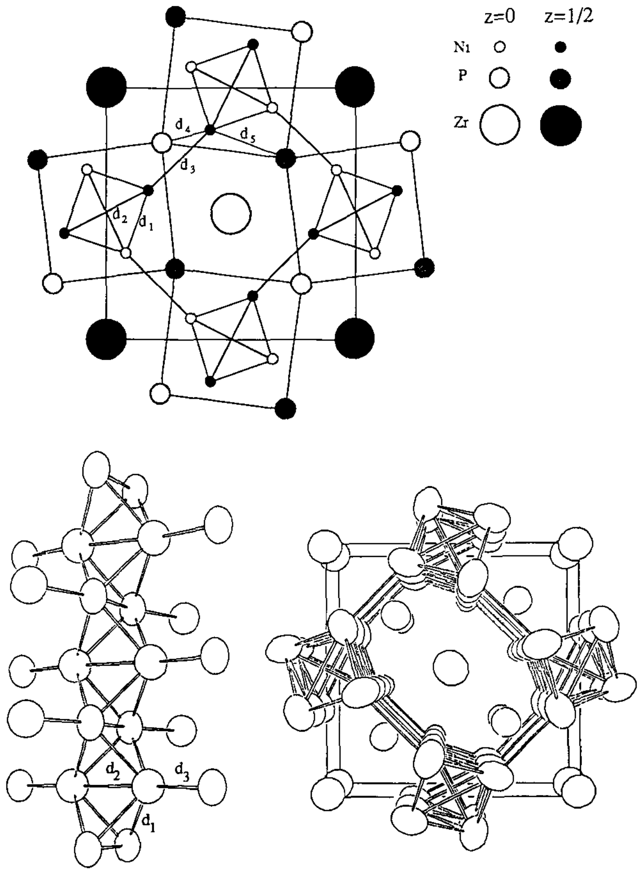

Fig. 1. Crystal structure of $ZrNi_4P_2$. In the upper part the structure is shown in a projection along the tetragonal axis. The Ni–Ni (d_1–d_3) and Ni–P (d_4, d_5) bonds are indicated. In the lower part the linkage within and between clusters is shown in both side and top views.

TABLE 1. Lattice constants and bond lengths of various $ZrFe_4Si_2$-type compounds

	Metal–metal				Metal–ligand	
	a/c	d_1 (Å)	d_2 (Å)	d_3 (Å)	d_4 (Å)	d_5 (Å)
$ZrNi_4P_2$	6.934 3.565	2.546	2.572	2.453	2.275	2.254
$TbNi_4P_2$	7.116 3.614	2.634	2.711	2.453	2.330	2.300
$DyNi_4As_2$	7.239 3.760	2.615	2.571	2.639	2.392	2.400
$ZrFe_4Si_2$	7.004 3.765	2.581	2.503	2.524	2.340	2.359
$ScFe_4P_2$	6.962 3.622	2.531	2.500	2.536	2.316	2.265

for the other compounds as follows: $Tb^{3+}|Ni_4P_2|^{3-}$, $Sc^{3+}|Fe_4P_2|^{3-}$ and $Zr^{4+}|Fe_4Si_2|^{4-}$. Consequently the number of electrons per M_4 cluster is 37 or 38 (Ni_4) and 28 or 29 (Fe_4). Moreover, since no metalloid–metalloid bonding occurs in any of these structures (more than 3 Å), one can attribute the formal charge −3 to phosphorus and arsenic and −4 to the silicon atoms.

In that structure, metal atoms display pseudotriangular coordination of three phosphorus atoms NiP_3 **1**, with the metal lightly out of the P_3 plane. In this pseudoplanar unit **1** two of the five d metal orbitals (in plane) are used to make metal–ligand bonds. The three other d orbitals (out of plane) are non-bonding with ligand orbitals and are therefore available to build up the metal–metal d_1, d_2 and d_3 bonds.

To date, no study has been carried out to describe how these metal orbitals develop the metal–metal network and particularly to rationalize the main factors which govern the observed variation occurring for metal–metal bond lengths in these compounds. Thus it appeared of interest to undertake a theoretical study in order to analyse the formation of metal–metal bonds, and especially to inquire into the role of the electronic configuration of the 3d transition element (nickel or iron), the nature of the ligand as well as that of the cation (zirconium, scandium, lanthanide). For this work, extended Hückel molecular orbitals (MOs) and tight-binding band structure calculations [10] have been carried out for $ZrNi_4P_2$ and then applied through a rigid band model [11] to the related compounds $DyNi_4As_2$, $TbNi_4P_2$, $ScFe_4P_2$ and $ZrFe_4Si_2$ (see Appendix A).

2. Molecular orbital interactions

As seen in Fig. 1, the d_1, d_2 and d_3 Ni–Ni bonds may be divided in two series: d_1, which corresponds to a metal–metal bond between two nickel atoms at different heights z and leads to the formation of linear chains $[Ni_4P_4]^1_\infty$ perpendicular to the |001| plane; bonds d_2 and d_3 lie in the |001| plane and correspond to intrachain and interchain bonds respectively.

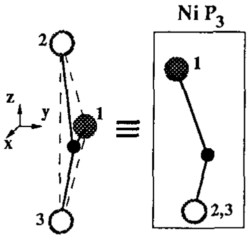

1

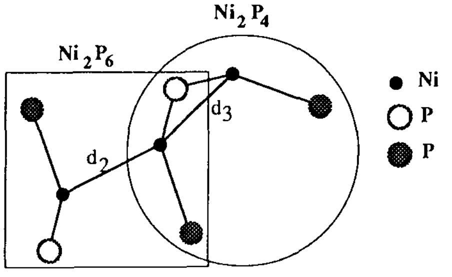

3 2

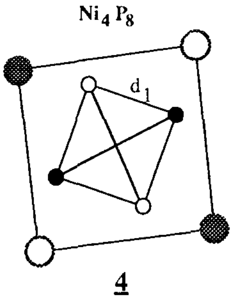

4

The formation of the intrachain (d$_2$) bond can be described from the study of the fragment Ni$_2$P$_6$ **2** which corresponds to a head-to-tail interaction of two NiP$_3$ units **1** with a d$_2$ metal–metal bond developing directly between the nickel atoms outside the plane of P$_3$ triangles. The interchain (d$_3$) bond can be studied through the fragment Ni$_2$P$_4$ **3**, this entity being obtained from the condensation of two triangular NiP$_3$ units **1** sharing one P–P edge; thereby the metal–metal d$_3$ bond develops through the two triangular P$_3$ planes.

The MO diagrams of these fragments are shown in Fig. 2. The main metal–metal interaction between two NiP$_3$ fragments is generated from the out-of-plane d$_{z^2}$ orbitals (1a′ MO) which present a good overlap in the metal–metal axis for both Ni$_2$P$_4$ (d$_3$) and Ni$_2$P$_6$ (d$_2$) fragments. This σ-type interaction induces a large energy splitting between bonding and antibonding MO components: 1a$_1$, 2b$_2$, (Ni$_2$P$_4$) and 1a$_g$, 2b$_u$ (Ni$_2$P$_6$). Metal–metal interactions with π- and δ-type character arising from 1a″ and 2a″ MOs are weaker but nevertheless notable for Ni$_2$P$_6$ (d$_2$ intrachain bond). On the contrary, this is not true for Ni$_2$P$_4$ (d$_3$ interchain bonds) where the large splitting between the 2a$_2$ and 2b$_1$ MOs, arising from the 2a″ MO of NiP$_3$, is mainly controlled by ligand–ligand interactions.

The d$_1$ bonds which lead to the formation of infinite $[\mathrm{Ni_4P_4}]^1_\infty$ chains can be analysed from the study of bonding in the Ni$_4$P$_8$ cluster **4** which can be seen as the condensation of two Ni$_2$P$_6$ **2** fragments. Figure 2 shows the MO diagram for Ni$_4$P$_8$ in relation to that of Ni$_2$P$_6$. As expected, one can see that σ-type orbitals of Ni$_2$P$_6$, which spread essentially in the |001| plane, have only a small part in the formation of d$_1$ bonds. Conversely the δ, δ^*, π, π^* orbitals of Ni$_2$P$_6$ which present a good extent and overlap along the |001| direction contribute to the main metal–metal interactions which generate d$_1$ bond formation. The bonding 2b, 2a and 1e MOs of Ni$_4$P$_8$ then arise mainly from π–π interactions (1a$_u$ MOs), $\delta^*+\delta^*$ interactions (2b$_g$ MOs) and $\delta \pm \pi^*$ interactions (1b$_g$, 2a$_u$ MOs) respectively. However, the S_4 symmetry group of the Ni$_4$P$_8$ unit involves some mixing between all the a-type orbitals as well as between the b-type orbitals. So a σ, π mixing is found again, for instance, in the 1b and 2b orbitals. In fact, all these main orbital interactions lead, at lower energy range, to six MOs (1b, 2b, 1a, 2a, 1e) which exhibit strong metal–metal bonding character and which correspond to the six bonds of the tetrahedral Ni$_4$ cluster present in Ni$_4$P$_8$.

3. Electronic band structures

3.1. The infinite chain $[Ni_4P_4]^1_\infty$

We first analyse the electronic structure and bonding of infinite linear chains $[\mathrm{Ni_4P_4}]^1_\infty$, the building block of the three-dimensional structure of ZrNi$_4$P$_2$, by carrying out extended Hückel tight-binding band structure calculations [10]. The energy bands obtained for the elementary cell **5** are shown in Fig. 3.

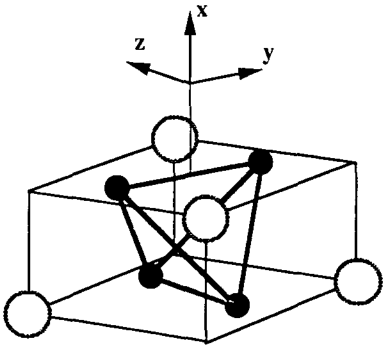

5

For this infinite system, the wavefunctions must be invariant with respect to translational symmetry. In the chain $[\mathrm{Ni_4P_4}]^1_\infty$, the group G_k of the wavevector k is (isomorphic with) the group C_{4h} at $k=0$ and π/a and the group S_4 along the line for the other values of k. At $k=0$ the bands are labelled according to their symmetry with respect to the y–z plane (S or A) and the 4_2 screw axis (+ or −). It should be noted that most of the bands are folded back at the zone edge ($k=\pi/a$) owing to the presence of a non-symmorphic operation, the 4_2 screw axis [12]. Then five a bands and five b bands, which derive from the five 5a and the five 5b MOs (see Fig. 2) of Ni$_4$P$_8$ are obtained. The lines that do not fold represent twofold degenerate bands which must be connected to the five e MOs seen in Fig. 2. The Fermi levels which have been calculated

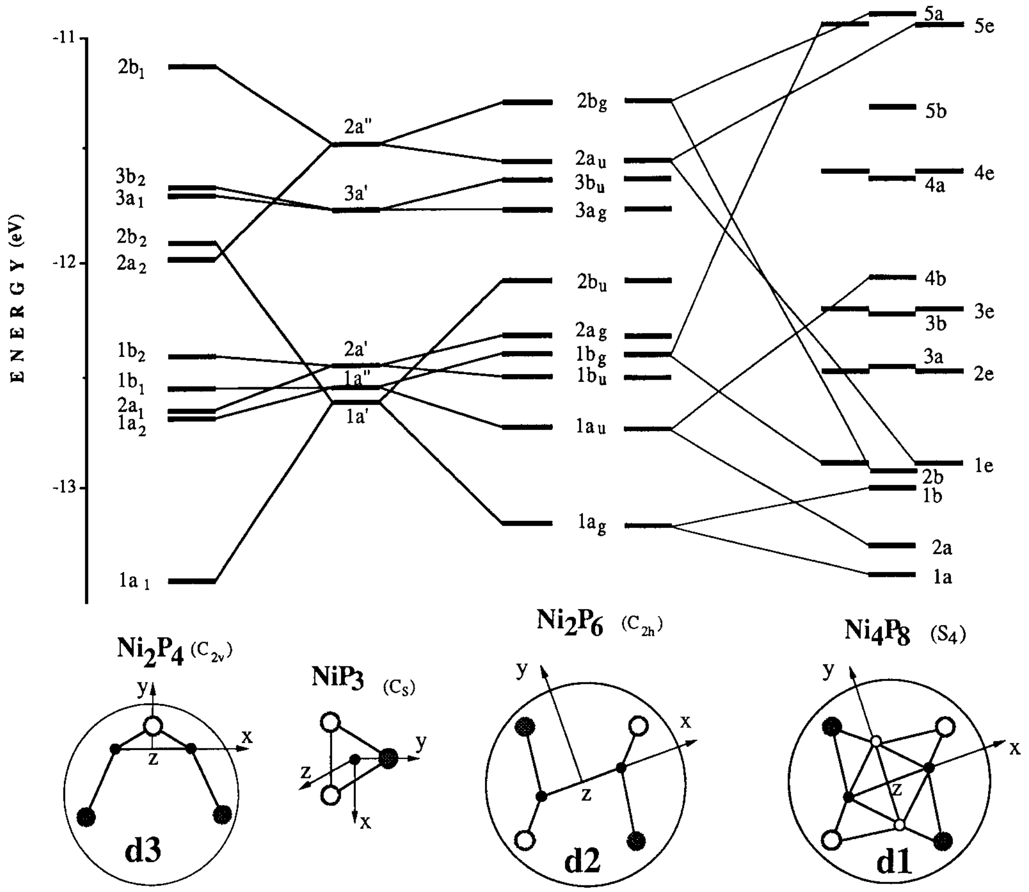

Fig. 2. MO diagrams of the fragments NiP_3, Ni_2P_4, Ni_2P_6 and Ni_4P_8 with correlation between them.

for the appropriate electron counts are indicated by the shaded zones. They occur in the upper part of the band diagram and cross dispersed bands, indicating metallic properties.

In order to deal with the bonding mechanisms within the chain, and to connect them to the MO interactions discussed above, Fig. 4 shows the total density of states (DOS) and the projected DOS (PDOS) on the σ, π, δ MOs of the Ni–Ni edge (d_2 bond) shared by Ni_4 tetrahedra along the chain. Moreover, the right-hand part of Fig. 4 displays, for the d_1 and d_2 bonds, the COOP curves [10], which indicated the averaged overlap population between two atoms *vs.* energy. For the d_2 bonds (perpendicular to the chain axis) the separation between the bonding and the antibonding character of the valence band nearly corresponds to that of σ and σ^* PDOS. It should be noted that the overlap of the π and σ PDOS is found to be in harmony with the π, σ mixing present in the MO diagram. As the energy goes up, the overlap of the σ, π and σ^*, π^* PDOS grows until the antibonding character dominates and leads to a strong antibonding character (σ^*, π^*, δ^*) near 12.2 eV. The upper part concerns mainly π^* and δ^* antibonding interactions. If we consider the d_1 bonds it is clear from the PDOS that its bonding character, in the lower energy range, arises from bands with metal–metal interactions of δ, π^* and δ^* character. At higher energy (near 10.5 eV) the strong antibonding band is also largely determined by $\delta+\pi^*$ interactions. All these bonding effects for the linear infinite chain agree well with the MO fragmentation approach previously discussed.

Finally, for the d_1 and d_2 bonds the averaged overlap populations, obtained from the integration of these COOP curves up to the Fermi level (Table 2), give an estimate of their strength. The weak values calculated for the electronic count of nickel result from the filled metal–metal antibonding bands in the upper part of the valence band. The loss of one electron per cluster only induces a weak increase in the overlap population for nickel- or iron-containing compounds while the loss of about 10 electrons per cluster from nickel to iron (Table 2) emphasizes this effect and approximately doubles the values.

3.2. *The tetragonal $ZrNi_4P_2$ structure*

After the study of isolated chains, we have now to consider the true experimental structure **8**. By using the infinite linear $|Ni_4P_4|^1_\infty$ chain **6** as a building block

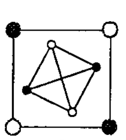

6

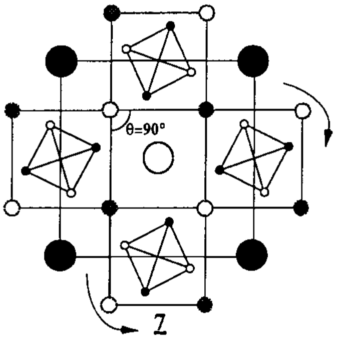

7

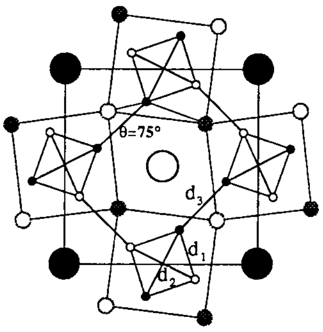

8

one can obtain the three dimensional tetragonal lattice of $ZrNi_4P_2$ as shown above.

We first bring together, in a symmetrical way ($\theta = 90°$), the chains **6** to form an extended model structure **7**. Thus the experimental structure **8** may be deduced, in a first approximation, by single rotation of the chains **6** around their axis as indicated since the cell parameters a of **7** and **8** are quite similar: if we take somewhat arbitrarily the a cell parameter to be 7.00 Å for **7**, we obtain 6.93 Å for **8**. This rotation induces a decrease in the θ angle from 90° in **7** to 75° in **8**, involving a shortening of the d_3 bond length from 2.61 Å to 2.45 Å.

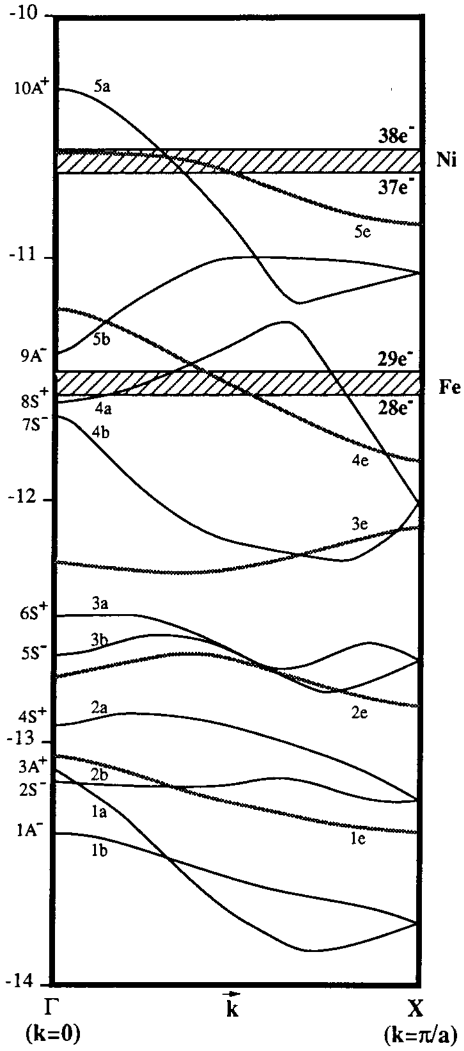

Fig. 3. Energy bands of the infinite chain $[Ni_4P_4]^1_\infty$.

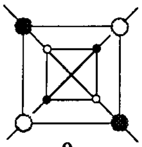

9

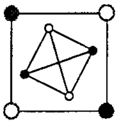

6

However, it is noteworthy that the building block **6** may be derived from a more symmetrical structure **9**. The route from **9** to **6** requires a single rotation of the $|Ni_4|^1_\infty$ chain around its axis within the $|Ni_4P_4|^1_\infty$ chain. This result leads to a lowering of symmetry (S_4 instead of D_{4h}). It should be noted that the crystal structures of Ni_3P, $Ni_{12}P_5$, Fe_3P and $Fe_{12}As_5$ exhibit the symmetrical chain **9** [13–15].

Finally, both rotations (**9**→**6** and **7**→**8**) contribute to the stabilization of the intra- and interchain metallic network and the cohesion of the structure.

Now we have to examine the relative importance of the major electronic effects on the stabilization of the experimental lattice. In order to mimic the distortion from **7** to **8**, we first carried out MO calculations on the Ni_2P_4 fragment **3** for various angles θ between 90° and 60°. The Walsh diagram of the 3d orbitals and the total energy curve are depicted in Fig. 5. Bonding levels (σ, π) stabilize with decreasing angle θ while antibonding levels (σ^*, π^*) are pushed upward. The electron counts lead to a partial filling of the $2b_1$ MO (nickel) or $3a_1$ MO (iron) which display a θ-independent energy. Therefore the energy gain from metal bonding MOs is counterbalanced by the energy loss of antibonding MOs. The metal–metal interactions and the electronic counts have, thus, little effect on the total energy minimum found for θ close to 75°. Nevertheless, this result is in agreement with the actual structure.

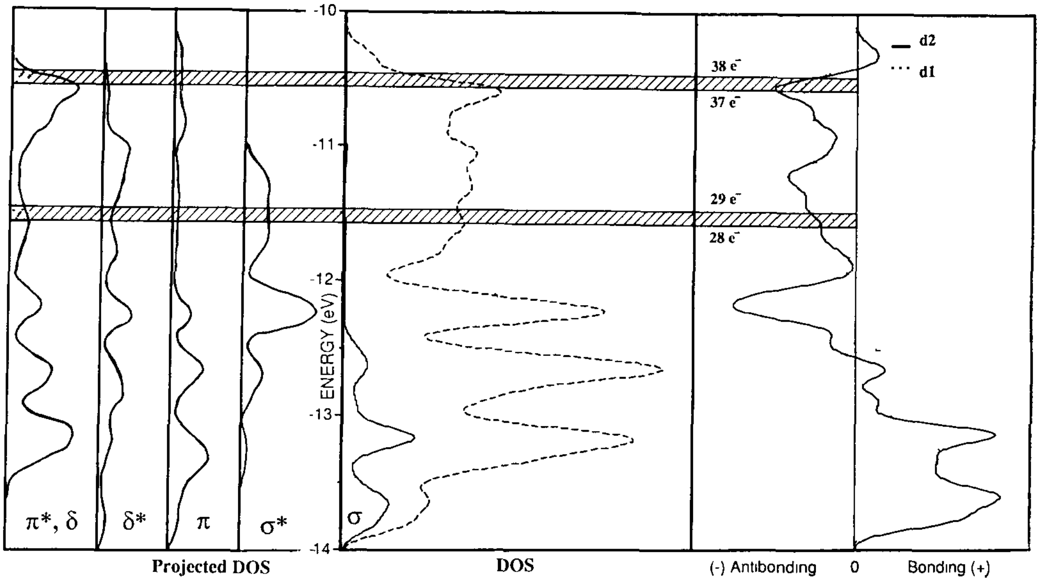

Fig. 4. DOS and PDOS for the Ni–Ni bonds within the condensed Ni_4 tetrahedra forming a chain. The σ, π and δ contributions to the Ni–Ni bonds along the common edges of the tetrahedra (d_2 bonds) are outlined on the left of the figure. – – –, total DOS for these interactions. At the right-hand side the crystal orbital overlap population (COOP) curves for the d_1 and d_2 bonds are shown.

TABLE 2. Overlap population indices for the Ni_4P_4 chain

Electrons per M_4 cluster	E_F (eV)	Overlap population indices for the following bonds	
		d_1	d_2
38	−10.58	0.054	0.044
37	−10.71	0.060	0.052
29	−11.54	0.105	0.101
28	−11.61	0.109	0.103

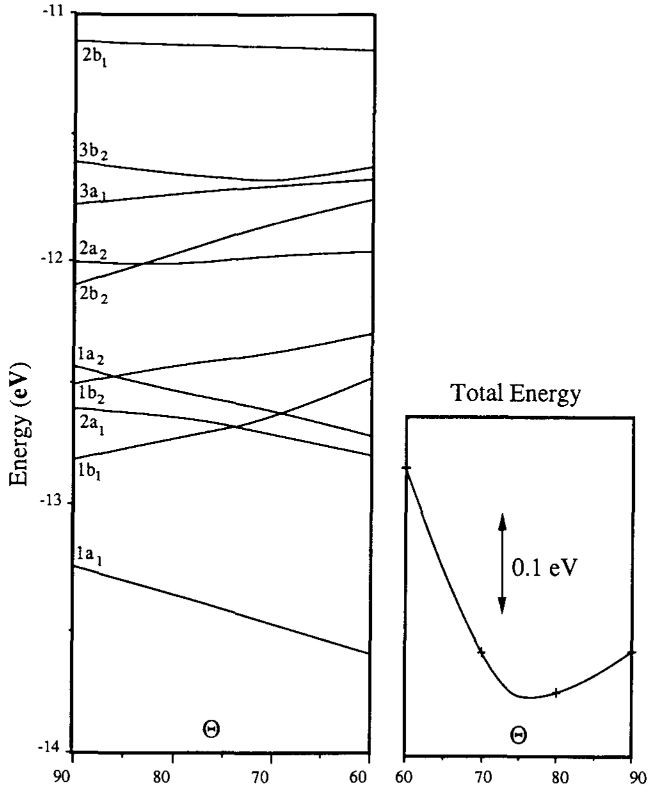

Fig. 5. Energy of the 3d orbitals of the Ni_2P_4 fragment **2** as a function of the angle θ. The total energy has a minimum at an angle $\theta = 75°$, in agreement with the crystal structure.

The bond length d_3 may then be largely controlled by an optimization of ligand–ligand repulsion. However, this first analysis does not take into account the interactions of the zirconium atoms and long-range interactions in extended structures.

Tight-binding band structure calculations have been performed for **7** and **8** at first without zirconium atoms. The energy bands for the main symmetry lines of the Brillouin zone are shown for **8** in Fig. 6. Only the upper energy 3d bands have been drawn. They are for electron counts of 28 electrons to 38 electrons per Ni_4 cluster.

The $P4_2mnm$ symmetry of the tetragonal cell induces a D_{4h} symmetry at the points Γ, Z, X and M of the Brillouin zone. The bands along the line ΓZ (C_{4v} symmetry) must be compared with those of the isolated chain **6** (Fig. 3). Compared with **6**, twice as many bands were found for **8** as well as a larger dispersion of the upper bands. On the other lines, especially ΓX and ΓM, the bands also display some dispersion proportional to the metal–metal interactions (d_2 and d_3 bonds). It must be noted that agrees with the large energy splitting obtained in Fig. 2 for the orbital interactions leading to the formation of the d_2 and d_3 bonds. Moreover,

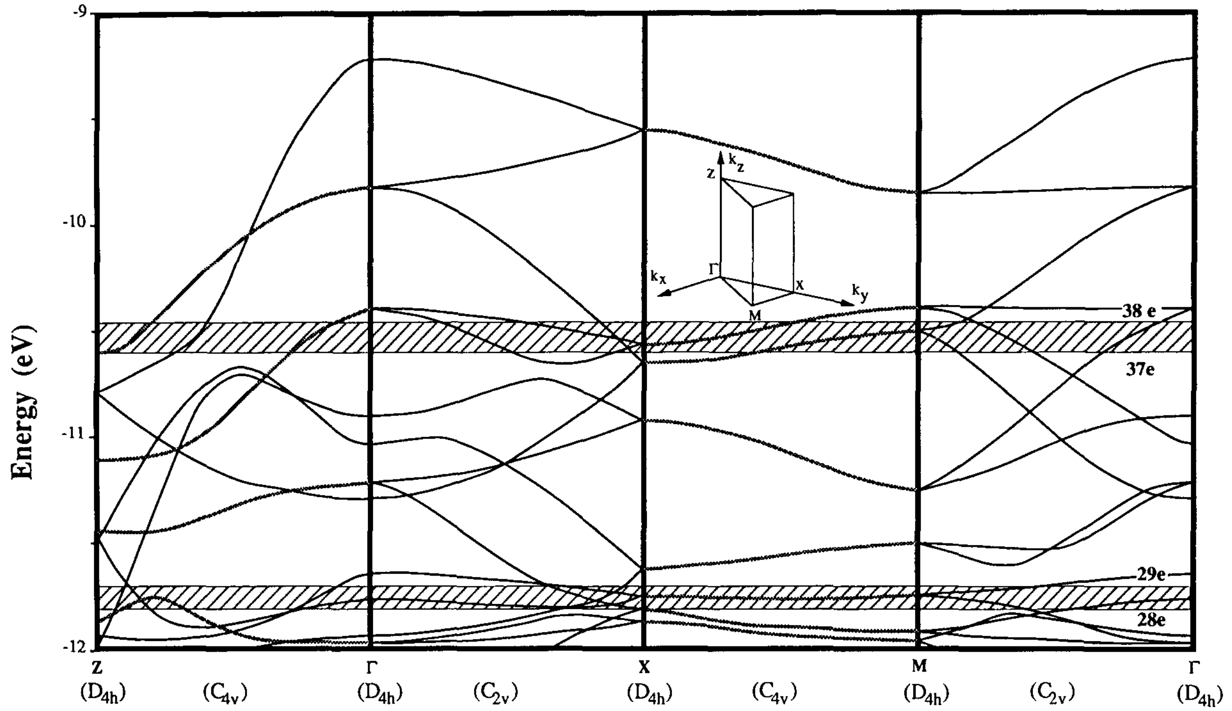

Fig. 6. Band structure for the extended solid ZrNi$_4$P$_2$ excluding the zirconium atoms.

in these extended systems the mixing with ligand bands enhances the band dispersions, especially for d$_3$ for which the upper part of the MO diagram, seen in Fig. 2, is governed by ligand–ligand interactions. The DOS and COOP curves of **8** depicted in Fig. 7 and the overlap populations collected in Table 3 enable one to discern the main features which result when chains are joined together. A slight modification of the shapes of the total DOS due to stronger overlap of bands is observed. The COOP curve of the d$_2$ bond presents a tangible evolution. Indeed, the strong antibonding character at the energy range centre has disappeared, while the bonding character has grown stronger at lower energy. These changes are expressed by the population values of Table 3.

The slight increase for nickel electron counts and the decrease for iron counts, when going from **6** to **7**, may suggest that the electronic effects associated with the interchain interactions lead to a compression of the Ni$_4$ tetrahedra in the chains and conversely to an expansion for the Fe$_4$ tetrahedra. The deformation from the model **7** to the experimental network **8** induces only a weak increase for all the electron counts. The same deformation obviously generates an increase in the overlap population of the d$_3$ bonds; however, we note, for the nickel configuration, that this population index remains the weakest although it corresponds to the shortest bond length d_3 (2.45 Å). This situation emphasizes the important role played by the ligand matrix in the d$_3$ Ni–Ni bond, in accord with the discussions from the MO diagram of Ni$_2$P$_4$ (Fig. 2) and the Walsh diagram on Fig. 5. For iron electron counts for the overlap populations of the d$_1$, d$_2$ and d$_3$ bonds are of the same order of magnitude.

Now let us return to the deformation which led from the chain **9** to the chain **6**. In **9**, the nickel atoms have tetrahedral coordination (ML$_4$) while in **6** they are in a triangular pseudoplanar group ML$_3$ since the fourth ligand is at a longer distance (L···ML$_3$). Extended Hückel MO energies are in favour of the ML$_4$ configuration, so the stabilization of ML$_3$ in **6** must result from interchain interactions in the three-dimensional lattice. The building up of the tetragonal structure **10** from chains **9** generates short interchain d$_3$ bonds (2.34 Å) with respect to twice the atomic radius (1.24 Å). So the rotation of the $|Ni_4|^1_\infty$ chain within **9** to form **6** may be attributed to the reduction of the metal–metal repulsion, especially so as the metal atoms have a large electron density.

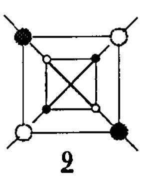

9

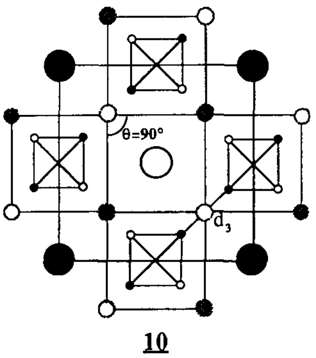

10

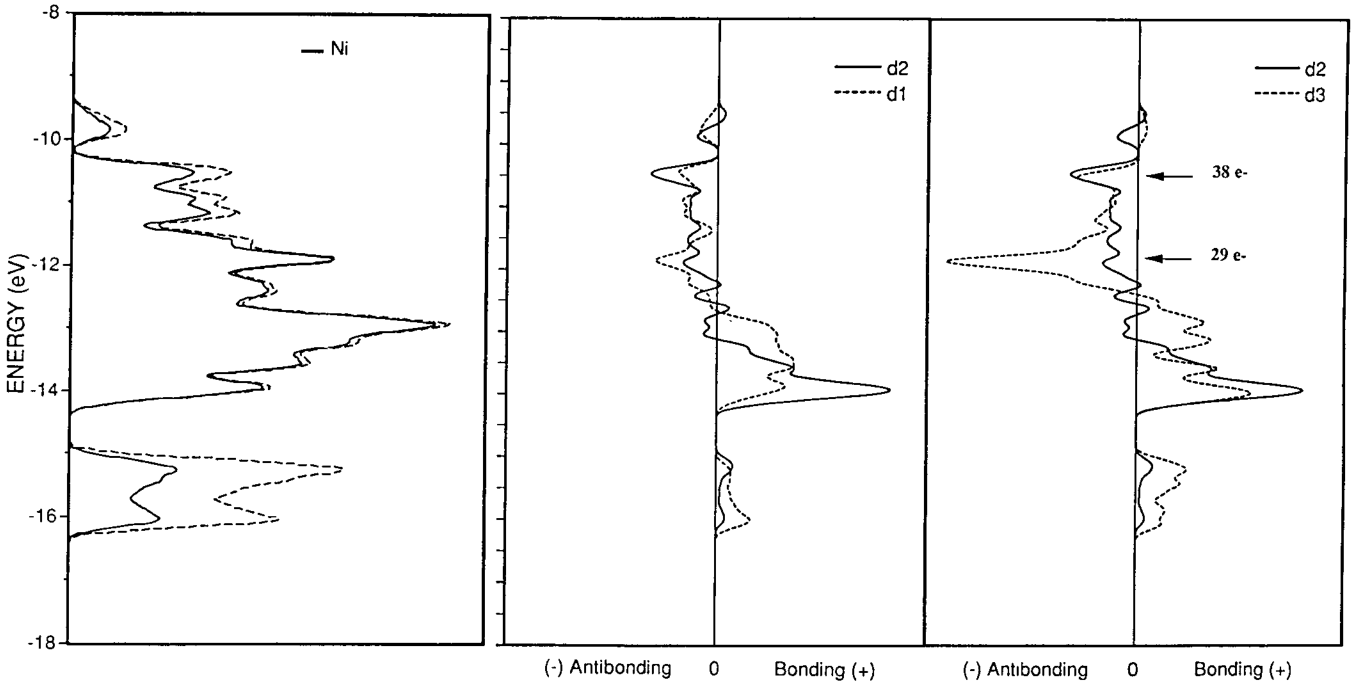

Fig. 7. DOS and COOP curves corresponding to the band structure of Fig. 6. At the left-hand side the total DOS for the extended solid Ni_4P_2 is shown (– – –), with the contribution of the nickel atoms (——). In the central and right-hand diagrams the COOP curves for the d_1, d_2 and d_2 bonds are drawn. The Fermi levels for the electron counts of 29 and 38 are indicated by arrows.

TABLE 3. Overlap population indices of **7** and **8**

Electrons per M_4 cluster	Structure	E_F (eV)	Overlap population indices for the following bonds		
			d_1	d_2	d_3
38	**7**	−10.50	0.061	0.052	0.011
	8	−10.46	0.062	0.053	0.042
37	**7**	−10.63	0.066	0.059	0.013
	8	−10.58	0.067	0.065	0.053
29	**7**	−11.79	0.097	0.102	0.069
	8	−11.73	0.101	0.104	0.105
28	**7**	−11.87	0.101	0.108	0.080
	8	−11.82	0.106	0.105	0.116

All our previous calculations considered a formal ionic interaction between the zirconium atoms and the $|Ni_4P_2|$ network with a full transfer of the four electrons of zirconium. In order to analyse this interaction better, calculations including the zirconium atoms in the elementary cell ($Zr_2Ni_8P_4$) have been performed. The DOS (Fig. 8) reveals bands of mainly zirconium character situated above the 3d metal and 3p ligand valence band. Nevertheless, it must be noted that the zirconium PDOS extends over the whole valence band and that the COOP curve for Zr–Ni exhibits bonding character at this energy range, which is the expression of an appreciable covalency. This is also expressed by the population index values calculated for the Zr–Ni interactions which are of the same order of magnitude as those of the metal–metal bonds d_1, d_2 and d_3.

It can be seen from Table 4 that the Zr–Ni population values do not vary much with the electron counts. This results from the fact that the bonding character of the zirconium interactions lies in the lower part of the valence band (Fig. 8). The comparison of values in Table 4 with those of **8** in Table 3 shows that the covalent interaction of zirconium induces a tangible reduction in the overlap populations of the d_3 bond while those of the d_2 bond increase. This effect on the d_3 population values suggests that the deformation within the chain (**9**→**6**) may result from a compromise between metal–metal repulsion and zirconium–metal bonding covalency. The d_1 bond which develops along the chain axis is less affected.

4. Concluding remarks

The main purpose of the present work was to provide a comprehensive description of the electronic structure of $ZrNi_4P_2$ in order to understand better the electronic effects on the bonding phenomena within the series of compounds with the $ZrFe_4Si_2$-type structure. So MO and tight-binding band structure calculations have been performed to build up, in a fragmentation approach, the electronic structure of the three-dimensional net-

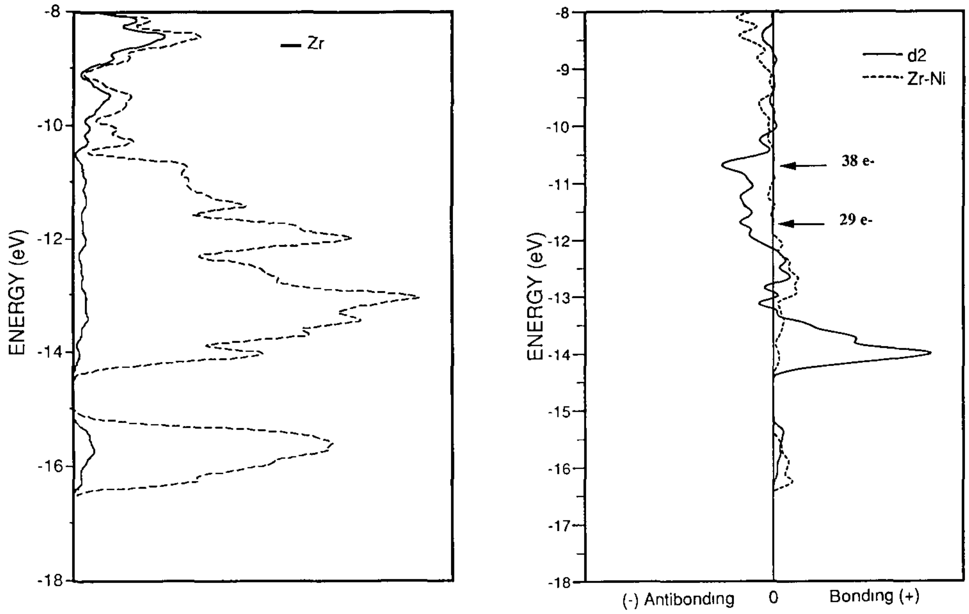

Fig. 8. DOS and COOP curves for $ZrNi_4P_2$. At the left-hand side the total DOS (– – –) with the contribution of the zirconium atom (——) is shown. The COOPs of the Zr–Ni interactions and the d_2 bonds are indicated in the other diagram.

TABLE 4. Overlap population indices for $ZrNi_4P_2$

Electrons per M_4 cluster	E_F (eV)	Overlap population indices for the following bonds			
		d_1	d_2	d_3	d(Zr–Ni)
38	−10.74	0.060	0.063	0.030	0.056
37	−10.89	0.065	0.074	0.040	0.056
29	−11.79	0.100	0.110	0.083	0.057
28	−11.85	0.104	0.111	0.094	0.057

work. The combination of these two complementary analyses enables one to point out the specific interactions which induce the bonding properties and to understand what, if anything, is special about the electron counts of these compounds. The evolution of the metal–metal overlap population when going from the electron count of nickel to that of iron suggests a shortening of the d_1, d_2 and d_3 bonds. This evolution agrees with the experimental results for the d_1 and d_2 intrachain bonds from $M'Ni_4P_2$ to $ScFe_4P_2$ (same ligand). For the experimental bond lengths d_3 of the nickel compounds, the inverse evolution is observed, which agrees with our theoretical study. Indeed this showed that, for nickel electron configurations, the variation in the bond lengths d_3 is essentially caused by the ligand–ligand and zirconium–metal interactions. In iron-containing compounds, the small change in the bond length d_3 from $ZrFe_4Si_2$ to $ScFe_4P_2$ confirms the theoretical prediction that metal–metal interactions have a more important effect in this series. Finally, the electronic structure of the compounds has been studied and discussed in some detail and the striking features have been explained by this single rigid band model approach.

References

1 Ya. P. Yarmolyuk, L. A. Lysenko and E. I. Gladyshevskii, *Dopov. Akad. Nauk Ukr. RSR, Ser. A, 3* (1975) 279.
2 Ya. F. Lomnitskaya and Yu. B. Kuz'ma, *Zh. Neorg. Khim., 31* (1986) 2412.
3 J. Y. Pivan, R. Guerin, E. H. El Ghadraoui and M. Rafiq, *J. Less-Common Met., 153* (1989) 285.
4 E. Ganglberger, *Monatsh. Chem., 99* (1968) 557.
5 R. Guerin, E. H. El Ghadraoui, J. Y. Pivan, J. Padiou and M. Sergent, *Mater. Res. Bull., 19* (1984) 1257.
6 E. H. El Ghadraoui, J. Y. Pivan, R. Guerin and M. Sergent, *Mater. Res. Bull., 23* (1988) 891.
7 S. I. Chikhrii, S. V. Orishchin and Yu. B. Kuz'ma, *Dopov. Akad. Nauk Ukr. RSR, Ser. A, 7* (1986) 81.
8 W. Jeitschko, L. J. Terbüchte, E. J. Reinbold, P. G. Pollmeier and T. Vomhof, *J. Less-Common Met., 161* (1990) 125.
9 T. Le Bihan, *Report of Diplôme d'Etudes Approfondies, Université de Rennes, June 1990.*
10 R. Hoffmann, *J. Chem. Phys., 39* (1963) 1397.
M.-H. Whangbo, R. Hoffmann and R. B. Woodward, *Proc. R. Soc. London, Ser. A, 366* (1979) 29.
11 R. Hoffmann, in *Solids and Surfaces: a Chemist's View of Bonding in Extended Structures,* VCH, New York, 1988.
12 G. Burns and A. M. Glazer, in *Space Groups for Solid State Scientists,* Academic Press, New York, 1978.

13 B. Aronsson, *Acta Chem. Scand., 9* (1955) 137.

14 S. Rundqvist and E. Larsson, *Acta Chem. Scand., 13* (1959) 551.

15 S. Rundqvist, E. Hassler and L. Lunqvist, *Acta Chem. Scand., 16* (1962) 242.

Appendix A

The bond distances used for the molecular orbital and band structure calculations were those of the experimental structure of $ZrNi_4P_2$ [A1]. The computations were carried out by using a tight-binding scheme implemented in the extended Hückel framework [A2]. The H_{ii} values are listed in Table A1. The band structures were obtained by solving the eigenvalue equations at six points for each symmetry line of the Brillouin zone. When an average quantity was computed (energy, overlap population) a mesh of 6*k* points inside the Brillouin zone was used.

TABLE A1. Parameters used for the calculations

	Orbital	H_{ii} (eV)	ξ_1	ξ_2	C_1[a]	C_2[a]
Ni	3d	−12.99	5.75	2.00	0.5683	0.6292
	4s	−8.86	2.10			
	4p	−4.90	2.10			
P	3s	−18.60	1.70			
	3p	−14.80	1.70			
Zr	4d	−10.20	3.835	1.505	0.6210	0.5769
	5s	−8.00	1.817			
	5p	−5.40	1.776			

[a] These are the coefficients in the double ξ expansion.

References for Appendix A

A1 J. Y. Pivan, R. Guerin, E. H. El Ghadraoui and M. Rafiq, *J. Less-Common Met., 153* (1989) 285.

A2 R. Hoffmann, *J. Chem. Phys., 39* (1963) 1397.
M.-H. Whangbo, R. Hoffmann and R. B. Woodward, *Proc. R. Soc. London, Ser. A, 366* (1979) 29.